


Magnetized granular particles running and tumbling on the circle S^1 M. Ledesma-Motolinía  and J. L. Carrillo-Estrada *Instituto de Física “Luis Rivera Terrazas”, Benemérita Universidad Autónoma de Puebla, Puebla 72570, Mexico*A. Escobar and F. Donado *Instituto de Ciencias Básicas e Ingeniería de la Universidad Autónoma del Estado de Hidalgo-AAMF, Pachuca, 42184, Hgo., México*Pavel Castro-Villarreal **Facultad de Ciencias en Física y Matemáticas, Universidad Autónoma de Chiapas, Carretera Emiliano Zapata, Km. 8, Rancho San Francisco, 29050 Tuxtla Gutiérrez, Chiapas, México*

(Received 13 September 2022; accepted 17 January 2023; published 17 February 2023)

It has been shown that a nonvibrating magnetic granular system, when fed by an alternating magnetic field, behaves with most of the distinctive physical features of active matter systems. In this work, we focus on the simplest granular system composed of a single magnetized spherical particle allocated in a quasi-one-dimensional circular channel that receives energy from a magnetic field reservoir and transduces it into a running and tumbling motion. The theoretical analysis, based on the *run-and-tumble* model for a circle of radius R , forecasts the existence of a dynamical phase transition between an erratic motion (disordered phase) when the characteristic persistence length of the *run-and-tumble* motion, $\ell_c < R/2$, to a persistent motion (ordered phase) when $\ell_c > R/2$. It is found that the limiting behaviors of these phases correspond to Brownian motion on the circle and a simple uniform circular motion, respectively. Furthermore, it is qualitatively shown that the smaller the magnetization of a particle, the larger the persistence length. It is so at least within the experimental limit of validity of our experiments. Our results show a very good agreement between theory and experiment.

DOI: [10.1103/PhysRevE.107.024902](https://doi.org/10.1103/PhysRevE.107.024902)**I. INTRODUCTION**

“Active matter” is a term conceived to classify those systems composed of entities (called *active particles*) that can extract free energy from a reservoir and transform it into kinetic energy; these particles transform into self-propelled units. The available reservoir can be on-board or environmental. The energy consumed by each active particle fuels an intrinsic mechanism that, in dissipating, transduces in a type of systematic motion that is generally common for all active particles [1–3]. The active matter can have a variety of patterns depending on its constituents that generate emergent and collective nonequilibrium phenomena [4,5], such as the patterns of dancing birds flocking in the sky [6] (other examples can be seen in Ref. [7]). This type of matter can also be presented at the sub-cellular scale [8–10], and it can have nonbiological components [4].

The constituents of active matter might be of a very diverse origin, from biological entities such as bacteria, unicellular protozoa, and spermatozoa, among many others, to artificial experimental models such as artificial microswimmers that mimic biological microorganisms such as Janus particles, colloidal propellers, Pt-loaded stomatocytes, and water droplets [2,11]. Some examples show self-propulsion can be carried out by converting chemical to mechanical energy. For instance, by coating with platinum, a hemisphere of a

polystyrene sphere immersed in a bank of hydrogen peroxide allows achieving a transition between directed motion to a Brownian motion using the platinum catalyst processes (this is a typical example of self-diffusiophoresis) [12]. Another illustrative example is a particle half-metal coated under laser irradiation that undergoes self-thermophoresis due to a local temperature gradient induced by a laser beam [13]. Some granular systems are examples of the physical realization of active matter [14–17], where the shape anisotropy of the single grains under vertical vibration can produce mobility on a horizontal surface [14]. For instance, the single-particle active motion can be generated in a vibrated granular system, where the main features of the Active Brownian Motion model have been proved in Ref. [18]. Furthermore, recent experimental studies on the dynamics of active granular particles have been performed using “microrobotic creatures,” a robot toy called “Hexbugs Nano” with an internal motor that produces vibrations, where the most outstanding properties of active motion are described through a Langevin stochastic model whence inertial effects are highlighted [19].

In contrast with the above vibrated granular systems, a nonvibrating granular system composed of many metallic balls under an alternating magnetic field is a simple 2D active matter system. Unlike a vibrated one, in which particles can move vertically, in a nonvibrating granular system, particles always remain in contact with the lower surface of the cell. This 2D granular system exhibits a ballistic behavior at short-times and a diffusive behavior at long-times as it is shown in Ref. [20], which is a feature of the stochastic dynamics

*pcastrov@unach.mx

of an active particle (for instance see Refs. [2,21]), including the dependence of the collective behavior on the confinement conditions, emerging also in vibrated granular systems [22], particle concentration, as well as the merging correlations that originate from self-organization phenomena like flocking, arrested structures, and crystallization [23–25]. The motion of particles during crystallization phenomena in confined conditions changes from diffusive to subdiffusive. In particular, it has been observed that confinement fastens the crystallization process [26,27], as well it induces complex correlations that, under certain conditions, generate emergent phenomena such as vortices or flocking [2].

Here, we wish to understand some of the main aspects of the stochastic dynamics of active granular matter confined in a quasi-1D-channel such as a circular track. We study this granular system based on a magnetized spherical bead activated by an alternating magnetic field used as a reservoir. The particle extracts energy from the magnetic field and transforms it into kinetic energy through the following mechanism. In the presence of the magnetic field, the magnetic dipole of the particle tries to align with the field to minimize the energy of the system. When the magnetic field reverses its direction, the particle rotates to align again with the field. In this process, a particle rotates, rolling over the surface without slipping because of kinetic friction. In this manner, the particle moves along the circular channel. When the field reverses direction again, a new impulse acts over the particle, making it continue rolling in the same direction or reversing the direction inside the channel to a random new direction leading to an active motion. If confinement were not present, the particle would change its motion to a random new direction leading to a 2D-active behavior [20].

One of the main aims of the present work is to understand how well the particle behavior of this nonvibrating 1D-granular-system can be described in terms of the *run-and-tumble* model [28–31] on the circle S^1 . In this model, the constraint to the line turns out in the continuous persistent random walk model introduced by Goldstein [32] back in the fifties, where the limiting process of the probability of finding a particle among a large number of noninteracting particles, that moves to the left or the right with equal probabilities and uniform velocity is described precisely by a solution of a telegrapher’s equation (TE). This equation arose as an approximation within the standard active Brownian motion model [21,33] studied in 2D flat space [34,35] and 2D curved surfaces [36]; and also in the *run-and-tumble* model for active particles [37,38]. However, for the 1D situation, the telegrapher’s equation description is exact, as opposed to the higher dimensions [38]; thus, its solutions have the full description of the active motion behavior. In particular, in contrast to a higher dimension, where the hydrodynamic-like description of the active dynamics consists of an infinite tower of a hierarchy of equations [38,39], the 1D case consists of the continuity equation and a current probability equation, namely,

$$\frac{\partial}{\partial t} \rho(s, t) = -\frac{\partial}{\partial s} \mathbb{J}(s, t), \quad (1)$$

$$\frac{\partial}{\partial t} \mathbb{J}(s, t) = -\frac{1}{\tau_c} \mathbb{J}(s, t) - v_0^2 \frac{\partial}{\partial s} \rho(s, t), \quad (2)$$

where τ_c is the average time elapsed before the particle performs a tumble, v_0 is the constant average persistence velocity, and s is the arc length of the curve. The quantity $\rho(s, t)$ represents the probability density function to find a particle at position s after a time t has passed, and $\mathbb{J}(s, t)$ is the current probability function that describes the preferential probability direction of the particle motion. The theoretical predictions of the *run-and-tumble* model on S^1 , described by Eqs. (1) and (2), predict the existence of a critical persistence length $\ell_c = v_0 \tau_c$ that distinguishes between two-state of motion; that is, the model predicts a dynamical phase transition between an erratic motion (disorder phase) to a persistent motion (order phase), where the extreme behavior of these states corresponds to a Brownian motion on the circle and a simple uniform circular motion, respectively. A good agreement between theory and experiment within the parameter regime considered in the experiment is shown below.

This paper is organized as follows: In Sec. II, the experimental setup to study the magnetic granular active motion in 1D is introduced; in particular, the main features of the stochastic motion of a magnetized ball confined on a circular channel and subjected to the time-varying magnetic field used as a thermal reservoir are described. In Sec. III the *run-and-tumble* model defined on a circle S^1 is developed; in particular, there is computed exactly the probability density function $\rho(s, t)$, the current probability function $\mathbb{J}(s, t)$. In Sec. IV, the expectation values of different physical quantities such as the mean-square displacement are calculated. In Sec. V, we give a comparison between the experimental results and the theoretical predictions made by the *run-and-tumble* model on S^1 . Here, we describe the most salient characteristic of a phase transition that undergoes the particle’s motion between an erratic and a soft motion; finally, in Sec. VI, we give our concluding remarks and perspectives.

II. EXPERIMENTAL SETUP

The experimental arrangement described in recent works [24,40–42] is slightly modified to study the stochastic motion of a metallic ball confined to a lithographic circular channel made on an acrylic plate. Briefly speaking, the setup consists of a pair of Helmholtz coils, where a flat and horizontal plate, called an observation cell, is placed in the homogeneous magnetic field region, as shown schematically on the left of Fig. 1. A closed circular channel is built on the observation cell, so the particle motion becomes confined into a quasi-1D-channel (see right-hand side of Fig. 1). The present experiment analyzes the motion of a single steel bead 1 mm in diameter. The coils are powered by a KEPCO brand power source controlled by a National Instruments data acquisition card through a sinusoidal signal generated by a homemade program in LabView. The coil system generates an oscillatory magnetic field of the form $B = B_0 \sin(2\pi ft)$. The frequency f is kept constant at 9.24 Hz. Recall that previously it has been shown that in this kind of system, the amplitude of the magnetic field B_0 , can be interpreted as an effective temperature, up to a proportional coefficient [23]. Therefore, for simplicity, the effective temperature is denoted here by B_0 , quantified in Gauss units denoted by G .

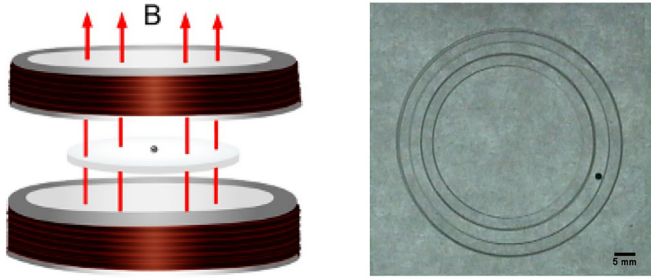


FIG. 1. Left: Experimental arrangement consists of a pair of Helmholtz coils that produce an oscillating magnetic field B through the observation cell. Right: A lithographic circular channel with a width value of 1.6 mm and one metallic bead of diameter $\sigma = 1$ mm. The channel radius is measured from the center of the channel to the center of the ball. The scale bar is 5 mm.

The experiments reported here start by putting a single particle in the quasi-1D-channel and turning on the alternating magnetic field. To search for the influence of the particle magnetization on the stochastic motion, it is prepared particles with magnetic dipole m_1 , obtained after exposing the particle under the magnetic field of magnitude 66 G for one hour, and particles with magnetic dipole m_2 , obtained by using a magnetic field of magnitude 100 G for the same time. Afterward, the mean-square displacement (MSD) is calculated to determine the stochastic motion behavior for particles with m_1 and m_2 , respectively. The MSD is defined by $\langle \Delta \mathbf{r}^2(t) \rangle = \langle |\mathbf{r}(t) - \mathbf{r}(0)|^2 \rangle$, where the displacement $\Delta \mathbf{r}$ is measured in particle's diameter units σ , and $\mathbf{r}(t)$ is the vector position measured from the center of the circular channel to the center of the metallic ball.

We carried out four series of experiments. In series S_1 , we used a particle with magnetic moment m_1 , a magnetic field amplitude $B_0 = 55$ G, and a set of various radii of the circular channel R , measured in units of the particle's diameter, σ . The ratio R/σ ranges from 5 to 34. For series S_2 , we used a particle with magnetic moment m_2 at the same values of B_0 and R as in S_1 . In the series S_3 , we used m_1 , circular track radius $R = 20 \sigma$, and varied the effective temperature, B_0 , from 44 to 88 G. For series S_4 , we used m_2 , circular track radius $R = 21 \sigma$, and varied B_0 from 11 to 88 G. In series S_3 , we observed at lower effective temperatures, 11 G, 22 G, and 33 G, that the particle tended to adhere to the wall and stop moving. The values of radii of the circular channel, R , and the effective temperature, B_0 for the experiment series S_1 , S_2 , S_3 , and S_4 are given in the Table I. At higher effective temperatures in S_3 and S_4 , the particle's kinetic energy might no longer be proportional to the field's amplitude, such that the amplitude could no longer be used as an effective temperature, as it is shown in Ref. [23].

Experiments were recorded using a CCD camera at a speed of 30 frames per second in interlaced AVI format. Each experiment lasted 5 min, enough time before the balls modified their magnetization. In the AVI video format, each frame is created using two fields, one after the other. The first with all the odd lines and the other with all the even lines. Frequently, slightly blurred particles are observed in the images. This effect is due to the speed with which they move; each field captures the

TABLE I. In this table we show the values of radii of the circular channel, R , and the effective temperature, B_0 for the experiment series S_1 , S_2 , S_3 , and S_4 .

Series	m	$R(\sigma)$								$B_0(G)$
S_1	m_1	5.0	9.0	13.0	14.0	21.0	25.0	29.0	34.0	55
S_2	m_2	5.0	9.0	13.0	14.0	21.0	25.0	29.0	34.0	55
		$B_0(G)$								$R(\sigma)$
S_3	m_1	44.1 55.2 66.7 77.3 88.4								20
S_4	m_2	11.0	22.0	33.1	44.1	55.2	66.7	77.3	88.4	21

particle in two different positions. A deinterlacing filter was used to improve the visual definition of the particle centers and increase the temporal resolution. In each field, made up of a pattern of lines with spaces, the missing information is interpolated to fill the pattern. Thus, a complete image is generated from each field. The final resolution obtained is 60 fps. The ImageJ package performed further analysis of the videos.

Figures 2(a) and 2(b) show the particle trajectories in a circular channel with $R = 34 \sigma$ for series S_1 at 20 s and 66 s, respectively. At the same time intervals, Fig. 2(c) and Fig. 2(d) show the particle trajectories for series S_2 . At a shorter time, it is observed that the particle in series S_1 exhibits more extensive traces and a larger displacement than the particle in the conditions of series S_2 ; clearly, this particle travels a smaller portion of the entire circular channel.

Figure 3(a) shows the mean-square displacement curves of the series experiment S_1 . It is observed there that each curve reaches a maximum value and then oscillates. The general trend is that the amplitude of the oscillations increases as

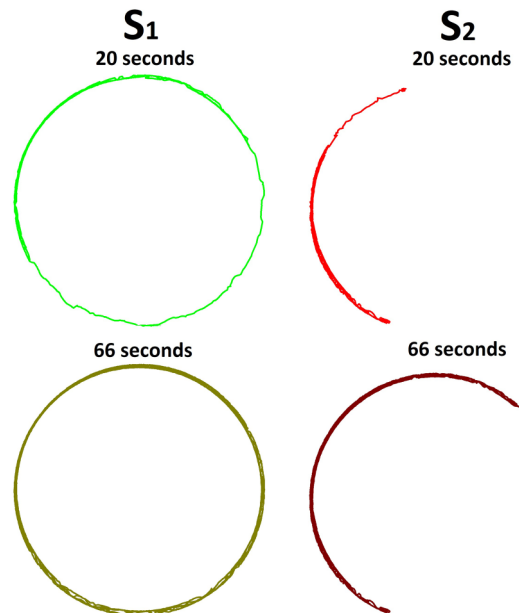


FIG. 2. Top-left particle trajectories at 20 s and down-left at 66 s for series S_1 are shown. Top-right, particle trajectories at 20 s and down-right at 66 s for series S_2 are shown. In both series, the radius of the circular track channel is $R = 34 \sigma$.

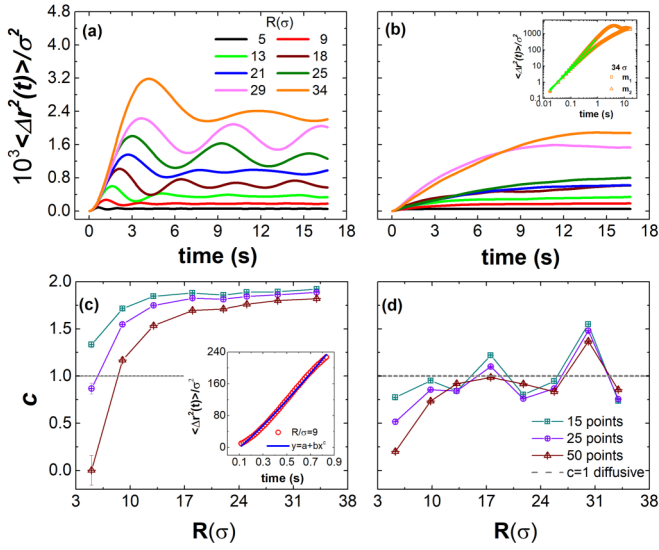


FIG. 3. Mean-square displacement for (a) series experiment S_1 and (b) series experiment S_2 for several radius R . Exponent c of the power law $\langle \Delta r^2(t) \rangle \propto t^c$, at the short-time regime of the curves (a) and (b), as a function of the radius R ; for (c) series S_1 and (d) series S_2 . Upper inset: log-log plot of the MSD for series S_1 and S_2 for $R = 34 \sigma$, the straight lines correspond to the power law of the first segment of MSD. Lower inset: Linear adjustment of the first segment of the red curve from (a) to calculate the exponent c . The exponent c is calculated by taking the first 15, 25, and 50 data points from the MSD, respectively.

long as R increases. Also, the maximum values appear to shift to the right as R increases. Both of these results can be explained considering the accessibility to more significant displacements when R increases and the fact that particle with magnetization m_1 presents itself as persistent motion as it is argued below at the conclusions. Figure 3(b) shows the corresponding curves from the series S_2 . These curves, which were obtained using a particle with larger magnetization, do not exhibit oscillations. They grow monotonically toward a limiting value. A direct explanation of this phenomenon can be obtained by observing the role of the magnetization of the particle, as shown in Fig. 2. Both regimes of the mean-square displacement can be compared on a log-log scale. The upper inset shows the MSD for series S_1 and S_2 considering $R = 34 \sigma$, the color line represents the power law adjustment by taking the first 50 points from the MSD. The initial portion of each set of MSD curves was fitted using power-law functions to determine the qualitative behavior of the stochastic motion. Figure 3(c) shows the exponents c obtained from each power-law function as a function of the radius. The behavior of the exponent corresponding to the series S_1 exhibits the same general trend for all the R values. The exponent indicates that the motion is superdiffusive with an exponent roughly of ~ 1.8 , considering a radius above 21σ . Figure 3(d) shows the corresponding c values as a function of radius. It was observed that the average value is around the unity, indicating that its motion is nearly diffusive for this magnetization of the particle.

Figure 4(a) shows the mean-square displacement curves obtained from the series S_3 . Here we varied the effective

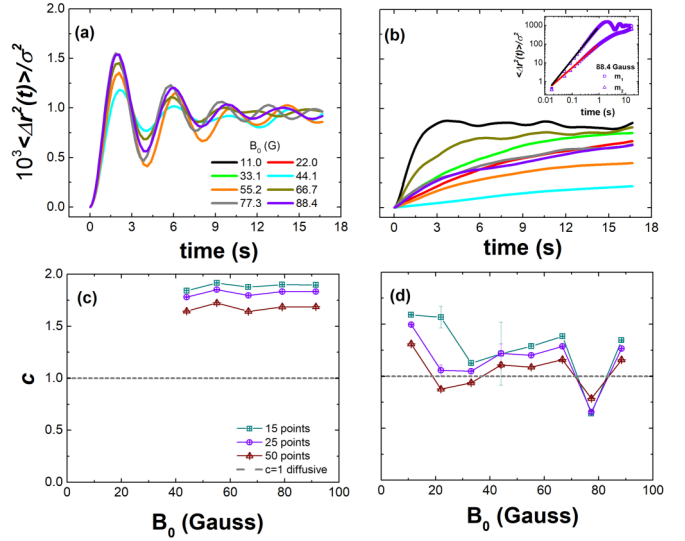


FIG. 4. Mean-square displacement for (a) series S_3 and (b) series S_4 as a function of the amplitude of magnetic field B_0 . Exponent c of the power law $\langle \Delta r^2(t) \rangle \propto t^c$, at the short-time regime of the curves (a) and (b), as a function of the radius R ; magnetic field B_0 for series S_3 (c) and series S_4 (d). The exponent c is calculated by taking the first 15, 25, and 50 data points from the MSD, respectively. Inset: log-log plot of the MSD for series S_3 , and S_4 at 88.4 G, the straight lines correspond to the power law of the first segment of MSD.

temperature, B_0 . As in series S_1 , each curve reaches a maximum value and oscillates. The general trend is that the amplitude of the oscillations increases with B_0 . The maximum values slightly shift to the left as B_0 increases. Figure 4(b) shows the corresponding curves of series S_4 . These curves, which were obtained using a particle with larger magnetization, grow almost monotonically toward a limit value, presenting as small superimposed oscillations. The comparison between both regimes of the MSD on a log-log scale at 88.4 G is shown in the inset, and the color line represents the power law adjustment by taking the first 50 points from the MSD. The exponents c obtained from each power-law function are shown in Fig. 4(c) as a function of the effective temperature B_0 . Although the exponent depends on the number of data used to fit, the general trend is the same. The motion is superdiffusive with an exponent of around ~ 1.8 . Figure 4(d) shows the corresponding c values as a function of effective temperature. In these conditions, the particle motion oscillates between superdiffusive to subdiffusive, with an average value above the unit indicating that the motion is also superdiffusive but less than in series S_3 .

The damping observed in the Figs. 3(a) and 4(a) is a consequence of the confinement since, after much time has passed, the probability density function to find a particle in a certain point of the circle is uniform and independent on time.

III. THEORY OF THE RUN-AND-TUMBLE MOTION ON THE CIRCLE $\rho(s, t)$ FOR THE ACTIVE MOTION ON S^1

We developed here the *run-and-tumble* model for a particle confined to move on a compact planar Jordan curve γ of perimeter L . In the simplest case of a one-dimensional

manifold γ , the possible states of an active particle are the motion to the right or the left. Mathematically, these states can be characterized as elements of a 0-dimensional sphere $S^0 = \{-1, 1\}$ accounting for the two directions of the particle velocity $\hat{v} = \pm 1$. Following the general model of *run-and-tumble* [28] for a particle in a d -dimensional curved manifold (A1) (see Appendix A), it is straightforward to obtain Goldstein's equations on γ [32],

$$\frac{\partial}{\partial t} P_+(s, t) + v_0 \frac{\partial}{\partial s} P_+(s, t) = -\lambda P_+(s, t) + \frac{\lambda}{2} \sum_{k=\pm} P_k(s, t), \quad (3)$$

$$\frac{\partial}{\partial t} P_-(s, t) - v_0 \frac{\partial}{\partial s} P_-(s, t) = -\lambda P_-(s, t) + \frac{\lambda}{2} \sum_{k=\pm} P_k(s, t), \quad (4)$$

where $P_{\pm}(s, t) = P(s, \hat{v} = \pm 1, t)$ represents the probability density function to move either to the right (+1) or to the left (-1), v_0 is the constant average particle velocity, and λ is a uniform tumbling frequency rate related to the persistent time defined by $\tau_c = \lambda^{-1}$, which gives the average time elapsed before the particle performs a tumble. Similarly, we also define the persistent length by $\ell_c = v_0 \tau_c$, meaning the average length run by the particle during the persistent time. One can use the radius of the circle R to define a large persistent length as $\ell_c \gg R$ and a small persistent length as $\ell_c \ll R$; thus, a useful dimensionless parameter shall be $\alpha = \ell_c/R$.

To solve Eqs. (3) and (4), it is convenient to define the marginal density of probability by $\rho(s, t) = \frac{1}{2}[P_+(s, t) + P_-(s, t)]$ obtained by integrating out the velocity directions, which represents the density probability of finding a particle at the position s at the time t . In contrast, the particle was at a certain initial position and time. In addition, we introduce the current density of probability by $\mathbb{J}(s, t) = \frac{v_0}{2}[P_+(s, t) - P_-(s, t)]$, taking into account the preferential probability direction of the particle motion. From these definitions, it is not difficult to get from Eqs. (3) and (4) the equations (1) and (2), which correspond to a continuity equation, and an exact current equation which gives the actual dynamics of the particle. Remark that Eq. (2) can be recast as

$$\frac{\partial}{\partial t} [e^{\frac{t}{\tau_c}} \mathbb{J}(s, t)] = -\frac{\partial}{\partial s} [v_0^2 e^{\frac{t}{\tau_c}} \rho(s, t)], \quad (5)$$

which represents a continuity equation for the conjugate quantities $\tilde{\rho}(s, t) = e^{\frac{t}{\tau_c}} \mathbb{J}(s, t)$ and $\tilde{J}(s, t) = v_0^2 e^{\frac{t}{\tau_c}} \rho(s, t)$. Now, Eqs. (1) and (2) can be easily decoupled in one-dimensional telegraphers equations [43] on the curve γ ,

$$\frac{\partial^2}{\partial t^2} \rho(s, t) + \frac{1}{\tau_c} \frac{\partial}{\partial t} \rho(s, t) = v_0^2 \frac{\partial^2}{\partial s^2} \rho(s, t), \quad (6)$$

where $\partial^2/\partial s^2$ represents the one-dimensional Laplacian associated with the one-dimensional space, where s is the arc length of the curve γ . Note that $P_{\pm}(s, t)$ and $\mathbb{J}(s, t)$ also satisfy similar telegraphers equations. Strictly speaking, $\rho(s, t)$ and $\mathbb{J}(s, t)$ depend on the initial position s' and the initial time $t = 0$. The initial conditions for the probability density function corresponding to $\lim_{t \rightarrow 0} \rho(s, t) = \delta(s - s')/L$, which expresses the fact that at time $t = 0$, the particle was

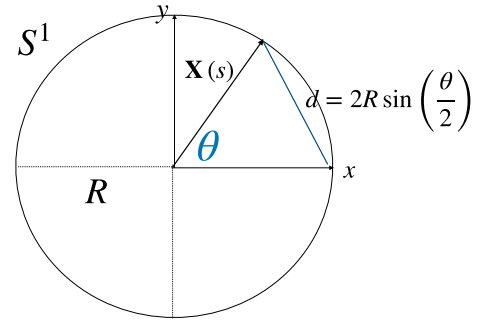


FIG. 5. Schematic image of a circle, S^1 , of radius R , with the embedding $\mathbf{X}(s) = (\cos \theta, \sin \theta)$, in the 2D Euclidean space with the usual Cartesian coordinates x, y . In addition, a chord of the circle is shown with length d as a function of the angle θ .

at the position s' ; and $\lim_{t \rightarrow 0} \partial \rho(s, t)/\partial t = 0$, which express that no particles are introduced at the initial time. Since we do not know the initial conditions for the current probability density, we proceed to solve for $\rho(s, t)$ and then use Eqs. (1) and (2) to find a solution for $\mathbb{J}(s, t)$.

The one-dimensional space γ can be described through a parametrization $\mathbf{X} : I \subset \mathbb{R} \rightarrow \mathbb{R}^2$ embedded in a two-dimensional Euclidean space. Although the following analysis can be carried out for any planar Jordan curve, in the following, we focus on a circular curve S^1 to adapt the theoretical predictions to the specific experimental conditions. The circle is described by the parametrization $\mathbf{X}(s) = R(\cos \theta, \sin \theta)$, where $\theta \in I = [-\pi, \pi]$, R is the radius of S^1 , and the arc length is $s = R\theta$ (see Fig. 5 for a schematic view of the circle). In this case, the Laplacian can be written simply as $\frac{1}{R^2} \frac{\partial^2}{\partial \theta^2}$, whose eigenfunctions are in the set $\{e^{im\theta} : m \in \mathbb{Z}\}$ and their eigenvalues are in $\{-\frac{m^2}{R^2} : m \in \mathbb{Z}\}$. The orthonormal relation is given by $\int_I d\theta e^{i(m-n)\theta} = 2\pi \delta_{mn}$ and the completeness relation, in this case, corresponds to $\delta(\theta - \theta') = \sum_{m \in \mathbb{Z}} e^{im(\theta - \theta')}$. In the following, we choose that at the initial time, the active particle is at $\theta' = 0$.

A. Probability density function $\rho(s, t)$ for the active motion on S^1

Here, we present the solution of the telegrapher's equation (6) with the appropriate initial conditions. The probability density function (PDF), $\rho(s, t)$, is written as a linear combination of the circular Laplacian eigenfunctions $\sum_{m \in \mathbb{Z}} \tilde{\rho}_m(t) e^{im\theta}$, where we identify $\tilde{\rho}_m(t)$ with *intermediate scattering function* (ISF) defined by

$$\tilde{\rho}_m(t) = \int_I ds e^{-im\theta} \rho(s, t), \quad (7)$$

for a particle confined to move on the circle S^1 , where we recall the arc length definition $s = R\theta$. The coefficients $\tilde{\rho}_m(t)$ satisfy the second order differential equation $\frac{d^2}{dt^2} \tilde{\rho}_m(t) + \tau_c^{-1} \frac{d}{dt} \tilde{\rho}_m(t) + m^2 \omega^2 \tilde{\rho}_m(t) = 0$, where it is convenient to define the frequency $\omega = v_0/R$, which allows us to write the dimensionless parameter $\alpha = \frac{\ell_c}{R}$ also as $\alpha = \omega \tau_c$. Thus, it is not difficult to show that the solution of the last differential equation is the linear combination $Ae^{-\frac{t}{\tau_c}(1-\sigma_m)} + Be^{-\frac{t}{\tau_c}(1+\sigma_m)}$,

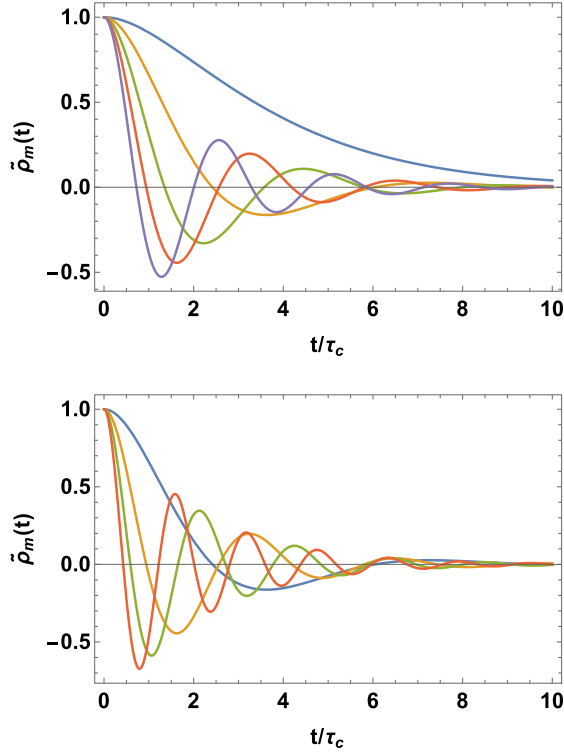


FIG. 6. Intermediate scattering function (ISF) [Eq. (8)] from the theory of *run-and-tumble*. Top: ISF for $m = 1$ [Eq. (11)], and for $m = 2, 3, 4, 5$ [Eq. (8)] with $\alpha < 1/2$. Down: ISF for $m = 1, 2, 3, 4, 5$ and $\alpha > 1/2$. Note that for both, top and down figures, bigger the m is, bigger the frequency that graph cross the time axis.

where $\sigma_m = \sqrt{1 - 4m^2\alpha^2}$, whose factors A, B can be obtained after imposing the initial conditions, which turns out to be $\tilde{\rho}_m(0) = 1/(2\pi R)$, and $\frac{d}{dt}\tilde{\rho}_m(0) = 0$. After a straightforward calculation, the ISF and the PDF are given by

$$\tilde{\rho}_m(t) = G\left(\frac{t}{2\tau_c}, 4m^2\alpha^2\right), \quad (8)$$

$$\rho(s, t) = \frac{1}{2\pi R} \left[1 + 2 \sum_{m=1}^{\infty} \cos(m\theta) G\left(\frac{t}{2\tau_c}, 4m^2\alpha^2\right) \right], \quad (9)$$

respectively, where the function $G(v, w)$ is given by

$$G(v, w) = e^{-v} \left[\cosh(v\sqrt{1-w}) + \frac{\sinh(v\sqrt{1-w})}{\sqrt{1-w}} \right]. \quad (10)$$

It is noteworthy to mention that the probability density function is given through a cosine Fourier series so that it is symmetric under the interchange $\theta \rightarrow -\theta$. The orthonormal basis, in this case, is given by $\{1/\sqrt{2\pi R}, \cos(m\theta)/\sqrt{\pi R}\}$, and its completeness relation is given by (C1). Finally, this Fourier series (9) is normalized with the perimeter of the circle, i.e., $\int_I ds \rho(s, t) = 1$, where the line element $ds = R d\theta$ and $I = [-\pi, \pi]$.

In Fig. 6, we explore the behavior of the ISF (8) against time scaled with the persistent time τ_c . Let us note in Eq. (8)

that for each m , there is a value for α where the intermediate scattering function transforms its behavior from monotonous to oscillating. This value can be determined by making $\sigma_m = 0$, which occurs when α acquires the values $1/(2m)$ for $m = 1, 2, \dots$. In particular, for $m = 1$, let us call $\alpha^* = 1/2$; thus, one can notice that ISF has an oscillating behavior for $\alpha > \alpha^*$ for each $m \in \{1, 2, \dots\}$; whereas for $\alpha \leq \alpha^*$ the ISF function has a monotonous behavior for the mode $m = 1$ and an oscillating one for the rest of the modes with $m > 1$. This analysis implies that for $\alpha > \alpha^*$ all the terms involved in the series of the probability density (9) have an oscillating behavior, whereas for $\alpha \leq \alpha^*$, the first term, with $m = 1$, is monotonous, while the remaining terms, for $m > 1$, have oscillating behavior. In particular, the ISF for the mode $m = 1$ at exactly $\alpha = \alpha^*$ is

$$\tilde{\rho}_{m=1}(t)|_{\alpha=\alpha^*} = e^{-\frac{t}{2\tau_c}} \left(1 + \frac{t}{2\tau_c} \right). \quad (11)$$

The previous analysis shown in Fig. 6 of the ISF Eq. (8) allows us to consider three dynamical states depending on the parameter α , namely, the *kinematic state* (KS), when $\alpha \gg 1$; *diffusive state* (DS), when $\alpha \ll 1$; and the *active state* (AS) in between the former and latter. Recall that $\alpha = \ell_c/R$; thus, KS means a considerable persistent length, whereas DS has a small persistent length. For the active state, we need to consider the full expression of the PDF Eq. (9). For the kinematic state, it is convenient to write $\tau_c = \alpha/\omega$, thus the leading term of the G function is $G(\omega t/(2\alpha), 4m^2\alpha^2) \simeq \cos(m\omega t)$, where the frequency $\omega = v_0/R$ is kept fixed. Now, after substituting in Eq. (9) and using Eq. (C1), one has that the probability density function in the KS corresponds to

$$\rho_k(s, t) = \frac{\delta(\theta - \omega t)}{R}. \quad (12)$$

In the kinematic state, this PDF represents a sharp pulse moving around the circle with uniform angular velocity $\omega = v_0/R$.

Now, for the diffusive regime, i.e., $\alpha \ll 1$, it is not difficult to show that G gives the asymptotic expression of $G(\omega t/(2\alpha), 4m^2\alpha^2) \simeq e^{-m^2 D_{\text{eff}} t/R^2}$, as long as the quantity $D_{\text{eff}} = v_0^2 \tau_c$ is kept fixed. Now, after substituting in Eq. (9), one has that the probability density function in the DS corresponds to

$$\rho_d(s, t) = \frac{1}{2\pi R} \left[1 + 2 \sum_{m=1}^{\infty} e^{-m^2 D_{\text{eff}} t/R^2} \cos(m\theta) \right]. \quad (13)$$

This probability density function corresponds to the PDF of a Brownian particle confined in a circle S^1 [44]. So now it makes sense to call D_{eff} effective diffusion coefficient.

B. Current probability density $\mathbb{J}(s, t)$

Here we present a solution for the current probability density $\mathbb{J}(s, t)$. Since we do not know the initial conditions of the current, we proceed to find an expression of the current using the solution for the probability density (9) and one of the equations (1) or (2). Following the development in Appendix B, the basic procedure consists of integrating Eq. (1) with respect to s and t . In addition, we choose that at the initial time $t = 0$, the particle is moving anticlockwise. Thus, the expression for

the current probability density is given by

$$\mathbb{J}(s, t) = \frac{2\omega^2\tau_c}{\pi} \sum_{m=1}^{\infty} m \sin(m\theta) F\left(\frac{t}{2\tau_c}, \sqrt{1-4m^2\alpha^2}\right) + \frac{\omega}{2\pi} e^{-\frac{t}{\tau_c}}, \quad (14)$$

where the function $F(v, w)$ is given by

$$F(v, w) = e^{-v} \frac{\sinh(v\sqrt{1-w})}{\sqrt{1-w}}. \quad (15)$$

For the active state, we need to consider the full expression (14) for the current probability. In the following, we determine the behavior of the current for the kinematic and diffusive states, respectively. In the KS $\alpha \gg \alpha^*$, one has the leading term of $F(\omega t/\alpha, 4m^2\alpha) \simeq \sin(\omega t)/(2m\alpha)$. Now, after substituting in Eq. (14) and using Eq. (C2), one has that the probability density function corresponds to

$$\mathbb{J}_k(s, t) = \omega \delta(\theta - \omega t), \quad (16)$$

which using Eq. (12), it can be written as $\mathbb{J}_k(s, t) = v_0 \rho_k(s, t)$ expressing the current of the sharp pulse moving with constant velocity v_0 around the circle.

Now, for the DS, i.e., $\alpha \ll \alpha^*$, it is not difficult to show that the asymptotic expression for F is given by $F(\omega t/\alpha, 4m^2\alpha) \simeq \frac{1}{2} e^{-D_{\text{eff}} t m^2/R^2}$ as long as D_{eff} kept is fixed. Now, after substituting in Eq. (14), the current has the asymptotic behavior

$$\mathbb{J}_d(s, t) = \frac{D_{\text{eff}}}{\pi R^2} \sum_{m=1}^{\infty} m \sin(m\theta) e^{-\frac{D_{\text{eff}} t m^2}{R^2}}. \quad (17)$$

Notice, as expected, that in this state, it satisfies the transport according to Fick's law $\mathbb{J}_d(s, t) = -D_{\text{eff}} \frac{\partial}{\partial s} \rho_d(s, t)$.

IV. EXPECTATION VALUES OF OBSERVABLES

In this section, we determine the expectation values of several physical observables using Eq. (9) to contrast with the experiment described above. In particular, we focus on the following quantities, namely, \hat{v} , the direction velocity; the normal vector $\mathbf{N} = (\cos \theta, \sin \theta)$; the tangent vector $\mathbf{T} = (-\sin \theta, \cos \theta)$; the Euclidean displacement $\Delta \mathbf{R} = \mathbf{X}(s) - \mathbf{X}(s')$, and the angular displacement $\Delta s = R(\theta - \theta')$. In what follows, we study the behavior of the mean values and mean-square values of these quantities for the three behaviors KS, AS, and DS.

A. Mean value of direction velocity \hat{v}

The stochastic variable \hat{v} gives the direction to the right (+) or the left (-) of the particle at each point on the circle. The mean value $\langle \hat{v} \rangle$ can be computed using the current probability $\mathbb{J}(s, t)$ as follows:

$$\langle \hat{v}(t) \rangle = \frac{1}{v_0} \int_1 ds \mathbb{J}(s, t). \quad (18)$$

Now, by direct calculation using Eq. (14), one has

$$\langle \hat{v}(t) \rangle = \begin{cases} 0, & \alpha \ll 1, \\ e^{-t/\tau_c}, & 0 < \alpha < \infty, \\ 1, & \alpha \gg 1. \end{cases} \quad (19)$$

Notice that at the diffusive state ($\alpha \ll 1$), the active particle motion does not have any preferential velocity direction. In the kinematic state, the average direction is exactly $\langle \hat{v} \rangle = 1$, consistent with the leading expression (16), meaning that in the KS, the particle moves anticlockwise for all the time, whereas in the active state, the particle on average moves also anticlockwise, however, it damped out exponentially as the time is increased.

B. Mean value of the geometrical quantities \mathbf{N} and \mathbf{T}

In the case of the circle, the normal vector is related to the vector position $\mathbf{N} = \mathbf{X}(s)/R$ and the tangent vector \mathbf{T} to the direction of the active particle vector velocity. Now, by direct calculation using Eqs. (9), (12), and (13), the expectation value of the normal vector is

$$\langle \mathbf{N}(t) \rangle = \begin{cases} e^{-D_{\text{eff}} t/R^2} \hat{\mathbf{x}}, & \alpha \ll 1, \\ G(t/2\tau_c, 4\alpha^2) \hat{\mathbf{x}}, & 0 < \alpha < \infty, \\ (\cos \omega t, \sin \omega t), & \alpha \gg 1, \end{cases} \quad (20)$$

where $\hat{\mathbf{x}}$ is unit vector along the x direction [see Fig. (5)]. Similarly, the expectation value of the tangent vector is $\langle \mathbf{T}(t) \rangle = \mathcal{R}_{\pi/2} \langle \mathbf{N}(s) \rangle$, where $\mathcal{R}_{\pi/2}$ is a ninety-degree anticlockwise rotation. Notice that no y component appears in $\langle \mathbf{N}(t) \rangle$ for the DS and AS, since, for these states, there is no preferential direction from the initial position; that is, the particle can move with the same probability to the right (+) or the left (-), while for the KS the particle undergoes a precise uniform circular motion with the frequency given by ω .

C. Mean value and mean-square value of Euclidean displacement

The Euclidean displacement $\Delta \mathbf{R}$ can be thought of as an *artificial* physical displacement because the active particle confined to the circle S^1 does not displace along the vector defined by $\Delta \mathbf{R}$. However, the Euclidean displacement is an observable measurable from an experimental point of view that captures the stochastic motion of the particle. The expectation value can be written in terms of $\langle \mathbf{N}(t) \rangle$ (20) as $\langle \Delta \mathbf{R}(t) \rangle = -R(\hat{\mathbf{x}} - \langle \mathbf{N}(t) \rangle)$. For the mean-square Euclidean displacement (MSED), $\Delta \mathbf{R}$ one has $(\Delta \mathbf{R})^2 = 2R^2(1 - \cos \theta)$, according to its thus it is enough to compute the expectation $\langle \cos \theta(t) \rangle$, but this quantity is given by $\langle \cos \theta(t) \rangle = G(t/2\tau_c, 4\alpha^2)$ as a consequence of the orthogonality of the terms in the Fourier series (9). Thus, the MSED is given by

$$\frac{\langle (\Delta \mathbf{R})^2(t) \rangle}{2R^2} = \begin{cases} 1 - e^{-\frac{D_{\text{eff}} t}{R^2}}, & \alpha \ll 1, \\ 1 - G\left(\frac{t}{2\tau_c}, 4\alpha^2\right), & 0 < \alpha < \infty, \\ 2 \sin^2\left(\frac{\omega t}{2}\right) & \alpha \gg 1. \end{cases} \quad (21)$$

This equation captures information on the stochastic motion of the particle confined to move on the circle. In the diffusive state ($\alpha \ll 1$), the MSED has the typical behavior of a Brownian motion on a compact curved manifold, whereas, for the kinematic state, the square root of MSD (21) can be interpreted as the average length d of the chord shown in the Fig. 5, consistent with uniform circular motion exhibited in this regime. Furthermore, in the active state, $0 < \alpha < \infty$, let

us note that similar to the ISF Eq. (8) that there is the value for $\alpha_* = 1/2$, where the mean-square Euclidean displacement transforms its behavior from a monotonous to an oscillating behavior. Thus, one can notice that the MSED has an oscillating behavior for $\alpha > \alpha^*$, and a monotonous one for $\alpha < \alpha^*$. The specific behavior of the MSED, monotonic or oscillating, gives a feature of a specific active particle with an intrinsic value of persistence length ℓ_c . In both diffusive and active states, the MSED reaches the limit value of

$$\langle \Delta \mathbf{R}^2(t) \rangle = 2R^2, \quad (22)$$

at the long-time regime; this value is known as the geometric limit [45] when there is a uniform probability density in each point of the circle. Indeed, assuming that the probability density in the long-time regime is uniform, i.e., $\rho \simeq 1/(2\pi R)$, thus, the mean-square Euclidean displacement is given by the elementary integral $\langle \Delta \mathbf{R}^2 \rangle \simeq \int_{-\pi}^{\pi} R d\theta [1/(2\pi R)] [2R^2(1 - \cos \theta)] = 2R^2$.

D. Mean value and mean-square value of angular displacement

The angular displacement $\Delta s = R\theta$ can be considered the *true* physical displacement because the active particle moves on the circle S^1 . Also, angular displacement is another observable measurable from an experimental point of view that captures the stochastic motion of the particle. Therefore, the expectation value is given by $\langle \Delta s(t) \rangle = 0$, which is expected since the probability density function is symmetric (9).

For the mean-square geodesic displacement (MSGD), $\langle \Delta s^2(t) \rangle$, we need to carry out integration by parts $\int_1^{\pi} \theta^2 \cos(m\theta) d\theta = 2(-1)^m/m^2$. By a straightforward calculation the MSGD $\langle \Delta s^2(t) \rangle$ is given by

$$\frac{\langle \Delta s^2(t) \rangle}{R^2} = \frac{\pi^2}{3} + 4 \sum_{m=1}^{\infty} \frac{(-1)^m}{m^2} \Phi_m(t, \alpha), \quad (23)$$

where

$$\Phi_m(t, \alpha) = \begin{cases} e^{-m^2 \frac{D_{\text{eff}} t}{R^2}}, & \alpha \ll 1, \\ G\left(\frac{t}{2\tau_c}, 4m^2 \alpha^2\right), & 0 < \alpha < \infty. \\ \cos(m\omega t), & \alpha \gg 1. \end{cases} \quad (24)$$

The mean-square angular displacement for the DS is consistent with previous works [44]. In addition, the expression for $\langle \Delta s^2(t) \rangle$ in the KS limit is consistent with the uniform circular motion shown in the above mean values since one can sum up the series in terms of the second Bernoulli polynomial [see Eq. (C3) in the Appendix], where it can be shown that $\langle \Delta s^2(t) \rangle = R^2(\omega t)^2$ for each t in the interval $[0, \pi/\omega]$, and then repeat the pattern with periods of 2π for $t > \pi/\omega$. In the active state, similar to the MSED, the mean-square geodesic displacement transforms its behavior from a monotonous ($\alpha < \alpha^*$) to an oscillating behavior ($\alpha > \alpha^*$). Similar to the MSED, in both diffusive and active states, the MSGD reaches the limit value of

$$\langle \Delta s^2(t) \rangle = \frac{\pi^2}{3} R^2, \quad (25)$$

at the long-time regime; this value is known as the geometric limit [44,46] when there is a uniform probability density at

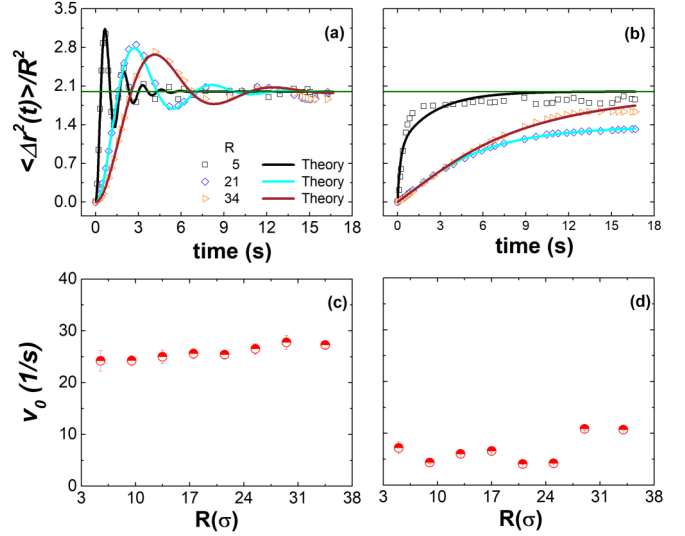


FIG. 7. (Top) Mean-square Euclidean displacement $\langle \Delta \mathbf{r}^2(t) \rangle$ for a particle confined in a circular channel from the experiment (open symbols) and *run-and-tumble* theory (solid lines). Three systems considered with radius $R/\sigma = 5, 21, 34$ at effective temperature $B_0 = 55$ G, (a) for magnetic moment m_1 (series S_1), and (b) for magnetic moment $m_2 > m_1$ (series S_2). The solid lines represent the theoretical prediction (21), adjusting the values of α and τ_c (see the Table II). The thin horizontal straight line is a reference guide for the eyes, showing the theoretical limit of value 2 [Eq. (22)]. (Down) Persistence velocity v_0 versus radius R , (c) for magnetic moment m_1 (series S_1), and (d) for magnetic moment $m_2 > m_1$ (series S_2).

each point of the circle. Indeed, assuming that the probability density in the long-time regime is uniform, i.e., $\rho \simeq 1/(2\pi R)$, thus, the mean-square geodesic displacement is given by the elementary integral $\langle \Delta s^2 \rangle \simeq \int_{-\pi}^{\pi} R d\theta [1/(2\pi R)] [R^2 \theta^2] = \frac{\pi^2}{3} R^2$.

V. RESULTS AND DISCUSSION

In this section, we compare the granular magnetic bead experiment described above in Sec. II and the theory of *run-and-tumble* on the circle S^1 developed in Secs. III and IV. To make this comparison, it has been chosen from the theory, the mean-square Euclidean displacement (MSED), $\langle \Delta \mathbf{R}^2(t) \rangle$, and the mean-square geodesic displacement (MSGD), $\langle \Delta s^2(t) \rangle$. Note that from an experimental point of view it is measured the MSD $\langle \Delta \mathbf{r}^2(t) \rangle$, which is strictly different from the MSED since the latter is computed exactly for the motion on the circle S^1 , while MSD captures radial motions since the channel has a finite-size. However, since the thickness of the channel is slightly bigger than the diameter of the particle, the following difference $\langle \Delta \mathbf{R}^2(t) \rangle - \langle \Delta \mathbf{r}^2(t) \rangle$ must be small. Angular displacement can be computed also from the experiment calculating $\theta(t) = \arctan[y(t)/x(t)]$, where $x(t)$ and $y(t)$ are extracted from the vector positions $\mathbf{r}(t) = [x(t), y(t)]$.

Figure 7(a) shows the comparison between the mean-square displacement, $\langle \Delta \mathbf{r}^2(t) \rangle$, using experiment series S_1 , with a particle with the lower magnetization m_1 , and the theoretical predictions encoding in equation $\langle \Delta \mathbf{R}^2(t) \rangle$ (21). It is observed that the fitted curves very closely reproduce

TABLE II. In this table we show the values for the parameter $\alpha = \ell_c/R$ and the persistence time τ_c obtained by adjusting Eq. (21) to the experimental values for the experiment series S_1 and S_2 .

$R(\sigma)$	S_1		S_2	
	α	τ_c (s)	α	τ_c (s)
5	2.812 ± 0.042	0.581 ± 0.009	0.261 ± 0.009	0.181 ± 0.013
9	2.325 ± 0.016	0.864 ± 0.006	0.292 ± 0.001	0.604 ± 0.003
13	2.866 ± 0.045	1.492 ± 0.024	0.286 ± 0.001	0.615 ± 0.003
18	3.182 ± 0.037	2.113 ± 0.026	0.278 ± 0.002	0.718 ± 0.004
21	1.756 ± 0.013	1.451 ± 0.013	0.158 ± 0.001	0.813 ± 0.001
25	2.211 ± 0.031	2.084 ± 0.031	0.147 ± 0.001	0.875 ± 0.001
29	1.586 ± 0.029	1.655 ± 0.035	0.297 ± 0.002	0.795 ± 0.004
34	1.522 ± 0.009	1.898 ± 0.013	0.288 ± 0.001	0.911 ± 0.002

the experimental results. A good experimental and theoretical agreement is also exhibited for the experiment series S_2 , with a particle with the higher magnetization m_2 , shown in Fig. 7(b). In both S_1 and S_2 , small discrepancies between the experiment and theory were notoriously observed in the case of a small radius $R = 5 \sigma$. These differences are attributed to the finite size of the channel thickness, which is slightly bigger than the diameter of the particle, implying that the radial degree of freedom of the bead is not entirely suppressed. In both series of experiments, the persistence velocity v_0 is calculated from a fit of Eq. (21) at the active state using the persistence time τ_c and the dimensionless quantity α as free parameters through the relation $\alpha = v_0 \tau_c / R$, for each radius R in the range R/σ from 5 to 34 (see Table II). In particular, all values of α in S_1 are larger than $1/2$, while in S_2 are smaller than $1/2$, according to the theoretical prediction. Figures 7(c) and 7(d) show the persistence velocity v_0 for the experiment series S_1 and S_2 , respectively. It is observed that for the system with magnetic moment m_1 , the particle persistence velocity v_0 slightly increased as R increases and roughly is a constant with a value around $25.7 \sigma/s$, whereas for the system with magnetic moment m_2 , the persistence velocity has a more abrupt behavior, and the increase is more pronounced. However, it has bigger oscillations around the value of $5 \sigma/s$. Additionally, the magnitude of persistence velocity v_0 is smaller for the higher magnetic dipole particle than for the smaller magnetic

dipole, which is the same trend observed in the experimental results discussed above in relation to Fig. 3.

Figure 8(a) shows the mean-square displacement for the particle with lower magnetization m_1 in a circle with radius $R = 20 \sigma$, and Fig. 8(b) for the particle with the higher magnetization m_2 in a circle with radius $R = 21 \sigma$, for the experiment series S_3 and S_4 , respectively. In both series, the magnitude of the amplitude of the magnetic field B_0 has varied from 11 G to 88.4 G. Also, both figures compare with the theoretical expression (21). It is observed that the fit between experiments and theory has a very good agreement. The persistence velocities v_0 were calculated from the values obtained with the fits (see Table III). In particular, all values of α in S_3 are larger than $1/2$, while in S_4 are smaller than $1/2$, according to the theoretical prediction. In these experiment series, small discrepancies between the experiment and theory can be observed in the small magnetic amplitude $B_0 = 11$ G and $B_0 = 44$ G (series S_3). These differences are also attributed to the small radial motion because the particle does not absorb enough energy from the magnetic field to self-propel along the circle. Figure 8(c) shows a weak dependence of v_0 on the effective temperature and roughly is a slight oscillation around $33.9 \sigma/s$. This is clear for the temperature's lowest and highest B_0 values. For the intermediate values, v_0 slightly increases as B_0 increases. The physical explanation of the fact that the highest effective temperature $B_0 = 88$ G, the value of v_0 decreases slightly because the magnetic interaction between

TABLE III. In this table we show the values for the parameter $\alpha = \ell_c/R$ and the persistence time τ_c obtained by adjusting equation (21) to the experimental values for the experiment series S_3 and S_4 . Notice that values $B_0 = 11, 22, 33$ G are absent in series S_3 since the reasons mentioned at Sec. II.

$B_0(\text{G})$	S_3		S_4	
	α	τ_c (s)	α	τ_c (s)
11			0.283 ± 0.014	0.450 ± 0.007
22			0.236 ± 0.001	0.888 ± 0.001
33			0.300 ± 0.001	0.850 ± 0.001
44	1.328 ± 0.025	0.828 ± 0.020	0.060 ± 0.002	0.964 ± 0.001
55	3.707 ± 0.100	2.367 ± 0.066	0.106 ± 0.001	0.867 ± 0.001
66	2.653 ± 0.027	1.634 ± 0.017	0.327 ± 0.002	0.609 ± 0.004
77	3.932 ± 0.037	2.348 ± 0.022	0.179 ± 0.001	0.794 ± 0.001
88	3.667 ± 0.026	2.293 ± 0.017	0.179 ± 0.001	0.822 ± 0.001

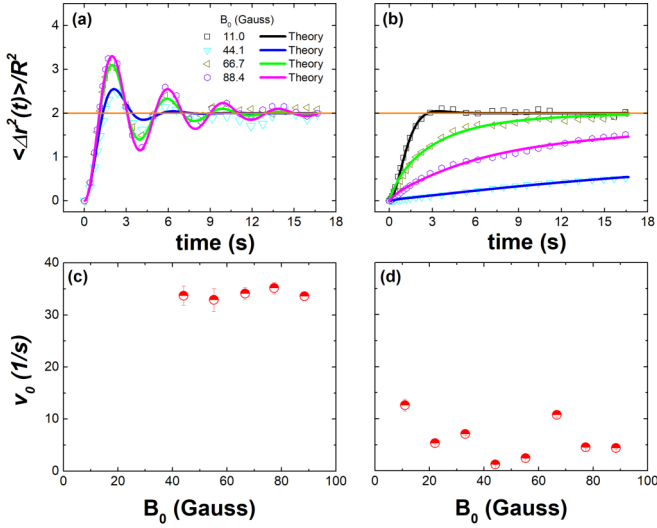


FIG. 8. (Top) Mean-square Euclidean displacement ($\langle \Delta \mathbf{r}^2(t) \rangle$) for a particle confined in a circular channel from the experiment (open symbols) and *run-and-tumble* theory (solid lines). Three systems considered with magnetic field $B_0 = 11$ G to $B_0 = 88.4$ G, (a) for magnetic moment m_1 (series S_3) with radius $R = 20 \sigma$, and (b) for magnetic moment $m_2 > m_1$ (series S_4) with radius $R = 21 \sigma$. The solid lines represent the theoretical prediction (21) adjusting the values of α and τ_c (see the Table III). The thin horizontal straight line is a reference guide for the eyes, showing the theoretical limiting value 2 [Eq. (22)]. (Down) Persistence velocity v_0 versus radius R , (c) for magnetic moment m_1 (series S_3), and (d) for magnetic moment $m_2 > m_1$ (series S_4)

the particle and the magnetic field is higher, so the particle exhibits more changes in its direction, leading to a more erratic motion. This behavior can also be observed in the experiment series S_4 , where the particle has higher magnetization. Figure 8(d) shows that persistent velocity v_0 has a more abrupt behavior and more extensive oscillations, with a general trend of decreasing as B_0 increases. At a low magnetic field, the particle travels longer paths, but as the magnetic field increases, the particle frequently changes direction, so the particle trajectory is more random. Thus, undoubtedly, the intensity of the interaction between the field and the particle magnetization has an important influence on the direction and inertial components of the particle motion; namely, it impacts the tumbling behavior that manifests in the erratic motion of the particle. Note that in both Figs. 7 and 8 can be observed the limit value $\langle \Delta \mathbf{R}^2(t) \rangle / R^2 = 2$ in the geometric regime.

Figure 9 compares the theoretical predictions and experimental results using the mean-square geodesic displacement $\langle \Delta s^2(t) \rangle$. It shows just three cases for the experiment series S_1 , S_2 , and S_3 , and four for the experiment series S_4 . This comparison considers only the dimensionless parameter, α , as a free parameter, whereas the persistence time, τ_c corresponds to the same value used to adjust the mean-square Euclidean displacement in the corresponding system. The curves of the mean-square geodesic displacement indicate that the fit between experimental data and theoretical prediction (23) has a good agreement. The general trend of the MSGD curves is similar to the corresponding Euclidean displacement case. In

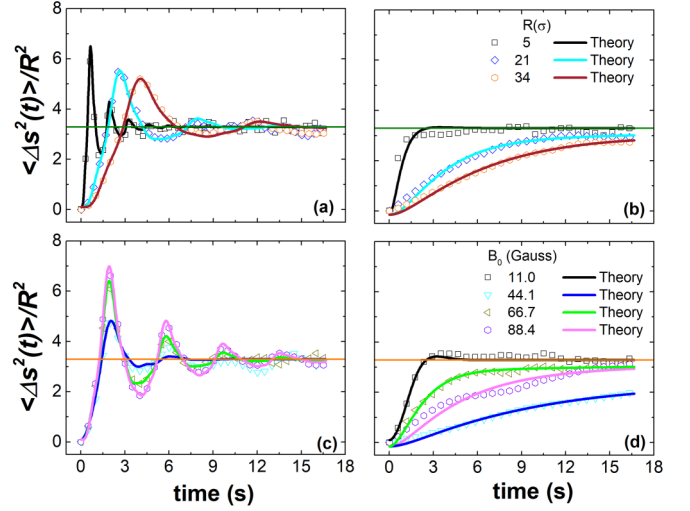


FIG. 9. Mean-square geodesic displacement ($\langle \Delta s^2(t) \rangle$) for a particle confined in a circular channel from the experiment (open symbols) and *run-and-tumble* theory (solid lines). Three systems considered with radius $R/\sigma = 5, 21, 34$ at effective temperature $B_0 = 55$ G, (a) for magnetic moment m_1 (series S_1), and (b) for magnetic moment $m_2 > m_1$ (series S_2). Additionally, four systems considered with magnetic amplitude $B_0/\text{G} = 11, 44.1, 66.7, 88.4$, (c) for magnetic moment m_1 (series S_3) with radius $R = 20 \sigma$, and (d) for magnetic moment $m_2 > m_1$ (series S_4) with radius $R = 21 \sigma$. The solid lines represent the theoretical prediction (23), adjusting the values of α . The thin horizontal straight line is a reference guide for the eyes, showing the value $\pi^2/3$ [Eq. (25)] of the geodesic geometrical limit.

the series S_1 , Fig. 9(a), and S_3 , Fig. 9(c), the maximum of the oscillations are higher than the corresponding Euclidean cases. Similarly, series S_2 , Fig. 9(b), and S_4 , Fig. 9(d), show similar behavior to the corresponding Euclidean cases. Additionally, the notorious difference between the MSGD and MSED is the geometric regime which in the geodesic case corresponds to the long-time regime to $\langle \Delta s^2(t) \rangle / R^2 = \frac{\pi^2}{3} \approx 3.28$.

Figures 10(a) and 10(b) show the comparison between the period, T , obtained as the ratio of the perimeter $2\pi R$ and the persistence velocity v_0 [whose values are extracted from Fig. 7(c)], and the period obtained directly from the experimental data corresponding to the mean-square displacements curves, measured from the beginning up to the first minimum, t_{\min} , for the experiment series S_1 and S_3 , respectively. It is observed that the values are very close to each other. Figure 10(a) shows that the period is linear with the radius, implying that persistence velocity for the particles with smaller magnetic moments does not depend on the radius of the circle. Figure 10(b) shows that the period only slightly depends on the effective temperature. Furthermore, a comparison between the persistence velocity obtained from the fitting through the theoretical model (21) and the velocity obtained as the ratio of the perimeter and the period obtained directly from the experiment are shown in Figs. 10(c) and 10(d). Again it is observed that in both series S_1 and S_3 , persistence velocity values are very close to each other. Figure 10(c) shows that the velocity slightly increases as the radius increases. Figure 10(d)

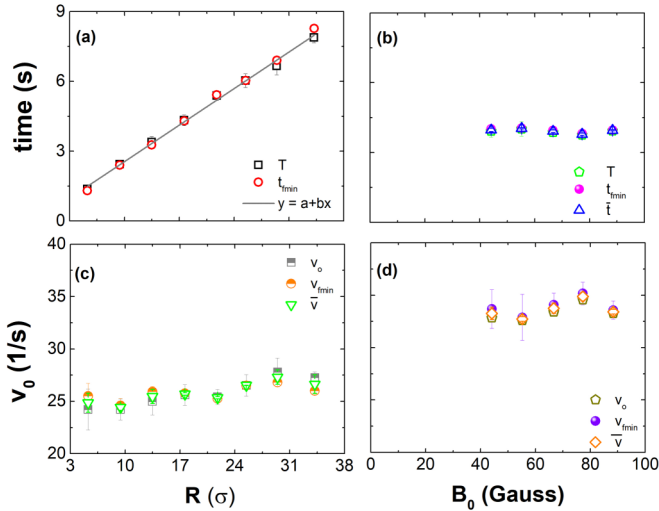


FIG. 10. Period of oscillation from the experiment (open circles symbols) and $T = 2\pi R/v_0$ where values of v_0 extracted from Fig. (7) as a function of the (a) radius of the circular channel, R , and (b) amplitude of the magnetic field. Persistence velocity v_0 as a (c) function of the radius of the circular channel, R , and (d) amplitude of the magnetic field B_0 .

shows that although the slight dependence of the persistence velocity on the effective temperature, one observes that v_0 oscillates around the value of $33 \sigma/s$. This irregular behavior of the persistence velocity can be understood as a consequence of the magnetic interaction between the field and the particle and the finite size of the channel's width, where the particle is confined.

VI. CONCLUSIONS

In this paper, we have investigated the random motion of an active particle confined along a circle through a nonvibrated granular experiment contrasting with the *run-and-tumble* model used to describe an active particle's stochastic motion. On the one hand, the experiment confines a magnetized metallic ball into a circular channel subjected to an alternating magnetic field that causes stochastic motion. In each experiment, the positions of the particle were determined after the data analysis of the recorded videos, which allows for calculating the mean-square displacement. On the other hand, we have developed the model of *run-and-tumble* to describe the self-propel motion of an active particle characterized by two parameters, namely, the persistence velocity v_0 and the tumble rate $\lambda = \tau_c^{-1}$, where τ_c is the persistence time. Using this model, we carried out an exact statistical physics analysis that allowed comparison with the experiment, finding a good agreement between the experimental results and the theoretical predictions.

The theoretical predictions of the *run-and-tumble* model on the circle established the existence of a transition between two states of motion: an erratic motion (or disordered phase) and persistent motion (or ordered phase). From the viewpoint of the theory, the change of the persistence length, $\ell_c = v_0\tau_c$, of a particle triggers a transition phase from a disorder to an

ordered phase. Notably, at the level of the MSD, the ordered phase is characterized by an oscillating function when $\ell_c > R/2$, while at the disordered phase, its behavior corresponds to an increasing monotonic function, for $\ell_c < R/2$, that saturates to a particular finite value due to the compactness of the circle. Additionally, from the theory, one can show that for $\ell_c \gg R$, the movement of the particle corresponds to a uniform circular motion, whereas for $\ell_c \ll R$, the movement corresponds to the usual Brownian motion on the circle.

From the experimental point of view, the magnetization m is the only essential property of the particle, and the oscillating behavior appears for particles with lower magnetization, while the monotonic behavior is for the higher value of magnetization. Thus, one can conclude qualitatively that the higher the persistence length of a particle is, the lower the magnetization, at least within the experimental limit of validity considered in the present experiment. Notably, a specific manifestation of the two states of motion predicted by the theory can be observed in Fig. 2 where particles with lower magnetization exhibit larger traces. In contrast, the particle with higher magnetization travels a smaller portion of the entire circular channel. One can explain the physical mechanism behind this dynamic transition through simple dimensional analysis. Indeed, introducing the characteristic period the particle changes its rotation direction $\tau_m = \sqrt{I/(mB_0)}$, where I is the particle's moment of inertia, and comparing it with the period the magnetic field alternates its direction $\tau_B = 1/f$ one can conclude that for the situation when $\tau_m > \tau_B$ the particle's magnetic torque maintains itself in the same direction giving rise to a bead's rolling motion with a more significant displacement along the circle as occurs in the persistent motion (or ordered phase), while if the magnetization increases above a critical value occurs $\tau_m < \tau_B$, which implies that the torque of the particle is constantly changing direction, that is generating a pronounce erratic motion (or the disordered phase). Additionally, it has been shown that the movement is superdiffusive, almost ballistic, in the order phase, while in the disordered phase, at a short-time regime, the motion becomes approximately diffusive. We have shown that this effect can be modulated by varying the particle-field interaction. As the interaction between the particle and magnetic field increases, the particle experiments more changes in its direction, going from a superdiffusive to a diffusive behavior. This interaction can be modulated by varying the magnetization of the particle, namely, by exposing it to a static magnetic field of different intensities or along different exposition times.

After comparing the theory and experiment, it has been shown that the magnetized metallic balls under the alternating magnetic field have the most salient properties exhibited by the active particle matter systems. This is because the magnetization of the ball corresponds to the intrinsic property in this case, and its interaction with the time-varying magnetic field allows the particle to extract energy to transform it into a self-propel motion along the quasi-1D circular channel. In particular, it has been shown that this granular nonvibrated experiment describes the main characteristics determined by the *run-and-tumble* model (initially to describe the bacterial motion [28]), at least in one-dimensional confinement in the absence of exclusion effects.

The present work can be extended in several directions. Using the same experiment setup, it remains to carry out an analysis using more than two different values of magnetizations to establish a quantitative law between the persistence length and the magnetization of the ball. Now that we have proved that the magnetized metallic balls behave as active particles, one can address the single-file diffusion problem of studying the interacting active particle system confined in quasi-1D circular channels. This analysis can be extended to investigate the universal character of the nature of the power law associated with the correlations observed experimentally in 1D colloidal systems [46]. Changing the experimental setup by replacing the circular channel with a concave surface plate allows addressing the problem of a single active particle moving in a 2D curved space [36,47]. For instance, using this kind of experimental setup one can board up the problem of triggering criticality phenomena in a single active particle in a spherical surface as predicted theoretically in Ref. [36]. Furthermore, at 1D, the telegrapher equation (6) is common in various models of active particles. However, the question remains to be answered: What is the most acceptable model to describe the stochastic motion of the magnetized active particle in higher dimensions? This could be addressed by considering in a 2D situation the Active Brownian Motion [21,33,36], the *run-and-tumble* model [28], and the Generalized Active Brownian Motion model proposed recently in Ref. [38].

ACKNOWLEDGMENTS

This work was partially funded with financial support by CONACyT, México, through Grants No. 731759 and No. A1-S-39909.

APPENDIX A: THE RUN-AND-TUMBLE MODEL IN MANIFOLDS

In this section, it is introduced the *run-and-tumble* model [28] for an active particle moving in a d -dimensional curved space \mathcal{M} . A particle that follows this model also has internal degrees of freedom that dictate the direction of motion according to the condition that the velocity is $\mathbf{v} = v_0 \hat{\mathbf{v}}$, where $\hat{\mathbf{v}} \in S^{d-1}$ and v_0 is a constant persistence velocity. Thus, the phase-space available for this particle corresponds to $\mathcal{M} \times S^{d-1}$. The model in the curved space is given by

$$\begin{aligned} & \frac{\partial}{\partial t} P(x, \hat{\mathbf{v}}, t) + v_0 \hat{\mathbf{v}} \cdot \nabla P(x, \hat{\mathbf{v}}, t) \\ &= -\lambda P(x, \hat{\mathbf{v}}, t) + \lambda \int_{S^{d-1}} \frac{d\hat{\mathbf{v}}}{V(S^{d-1})} P(x, \hat{\mathbf{v}}, t), \end{aligned} \quad (\text{A1})$$

where $\{x^a\}$ with $a = 1, \dots, d$, represents a set of local coordinates and $\hat{\mathbf{v}} \cdot \nabla f = \frac{1}{\sqrt{g}} \hat{v}^a \partial_a (\sqrt{g} f)$, where g is the determinant of the tensor metric g_{ab} that defines the Riemannian geometry of the space \mathcal{M} , and $V(S^{d-1})$, and $V(S^{d-1})$ is the volume of the sphere S^{d-1} . In the above model, λ is the tumbling rate that gives, on average, how many tumbles the particle makes in a unit of time.

In the simplest case, when $d = 1$, the sphere S^0 has only two points, $S^0 = \{-1, 1\}$, that are interpreted as the direction to the left (-1) or the right ($+1$), the volume $V(S^0) = 2$,

and the integration is given adopting the formal expression $\int d\hat{\mathbf{v}} f(\hat{\mathbf{v}}) = f(+1) + f(-1)$. From this definition, we define the probability density function $\rho(s, t)$ and the current probability function

$$\rho(s, t) = \int_{S^0} \frac{d\hat{\mathbf{v}}}{V(S^0)} P(s, \hat{\mathbf{v}}, t), \quad (\text{A2})$$

$$\mathbb{J}(s, t) = \int_{S^0} \frac{d\hat{\mathbf{v}}}{V(S^0)} \hat{\mathbf{v}} P(s, \hat{\mathbf{v}}, t). \quad (\text{A3})$$

APPENDIX B: CALCULATION OF THE CURRENT PROBABILITY DENSITY $\mathbb{J}(s, t)$

Here, we present a calculation for the current probability density $\mathbb{J}(s, t)$. We proceed to find an expression of the current using the solution for the probability density (9) and Eqs. (1) and (5). Let us calculate the partial derivative of $\rho(s, t)$ with respect to time, that is,

$$\frac{\partial \rho}{\partial t} = -\frac{2\alpha^2 e^{-\frac{t}{2\tau_c}}}{\tau_c \pi R} \sum_{m=1}^{\infty} \cos(m\theta) \frac{m^2 \sinh\left(\frac{t}{2\tau_c} \sqrt{1-4m^2\alpha^2}\right)}{\sqrt{1-4m^2\alpha^2}}. \quad (\text{B1})$$

Now, in virtue of continuity equation (1), we equate the last expression to $-\frac{1}{R} \frac{\partial \mathbb{J}}{\partial \theta}$. Afterward, we integrate out the variable θ such that

$$\begin{aligned} \mathbb{J}(s, t) &= \frac{2\omega^2 \tau_c e^{-\frac{t}{2\tau_c}}}{\pi} \sum_{m=1}^{\infty} m \sin(m\theta) \frac{\sinh\left(\frac{t}{2\tau_c} \sqrt{1-4m^2\alpha^2}\right)}{\sqrt{1-4m^2\alpha^2}} \\ &+ \psi(t), \end{aligned} \quad (\text{B2})$$

where $\psi(t)$ is a time function to be determined. To obtain $\psi(t)$, we observe that the current can also be obtained using Eq. (5). Thus, we calculate $\partial \rho / \partial s$, namely,

$$\frac{\partial \rho}{\partial s} = -\frac{1}{\pi R^2} \sum_{m=1}^{\infty} m \sin(m\theta) G\left(\frac{t}{2\tau_c}, 4m^2\alpha^2\right). \quad (\text{B3})$$

Now we integrate out the time variable t on both sides of Eq. (5) such that we obtain for the current

$$\begin{aligned} \mathbb{J}(s, t) &= \frac{2\omega^2 \tau_c e^{-\frac{t}{2\tau_c}}}{\pi} \sum_{m=1}^{\infty} m \sin(m\theta) \frac{\sinh\left(\frac{t}{2\tau_c} \sqrt{1-4m^2\alpha^2}\right)}{\sqrt{1-4m^2\alpha^2}} \\ &+ \varphi(s) e^{-\frac{t}{\tau_c}}. \end{aligned} \quad (\text{B4})$$

Now, comparing both expressions (B2) and (B4) of the current, one can conclude that $\varphi(s) = \mathbb{J}_0$ is a constant independent of s and $\psi(t) = \mathbb{J}_0 e^{-\frac{t}{\tau_c}}$. The constant \mathbb{J}_0 is determined by noting that the integration of the series term in Eq. (B4) vanished then $\int_I ds \mathbb{J}(s, t) = 2\pi R \mathbb{J}_0 e^{-\frac{t}{\tau_c}}$, now observing that $\int_I ds \mathbb{J}(s, t) = v_0 \langle \hat{\mathbf{v}}(t) \rangle$. Now let us choose that at $t = 0$ the direction is such that $\langle \hat{\mathbf{v}}(0) \rangle = 1$, thus one has $v_0 = (2\pi R) \mathbb{J}_0$, thus $\mathbb{J}_0 = v_0 / (2\pi R)$. Finally, we got the desired result (14).

APPENDIX C: USEFUL MATHEMATICAL IDENTITIES

The following mathematical identities were useful for the analytical calculations:

$$\frac{1}{2\pi R} \left(1 + 2 \sum_{m=1}^{\infty} \cos(m\theta) \cos(m\theta') \right) = \frac{1}{R} \delta(\theta - \theta'), \quad (\text{C1})$$

$$\frac{1}{2\pi R} \left(1 + 2 \sum_{m=1}^{\infty} \sin(m\theta) \sin(m\theta') \right) = \frac{1}{R} \delta(\theta - \theta'), \quad (\text{C2})$$

$$\sum_{m=1}^{\infty} \frac{(-1)^m}{m^2} \cos(my) = \pi^2 B_2 \left(\frac{y}{2\pi} - \frac{1}{2} \right), \quad (\text{C3})$$

where $B_2(x) = x^2 - x + \frac{1}{6}$ is the second Bernoulli polynomial.

-
- [1] M. C. Marchetti, J. F. Joanny, S. Ramaswamy, T. B. Liverpool, J. Prost, M. Rao, and R. A. Simha, *Rev. Mod. Phys.* **85**, 1143 (2013).
- [2] C. Bechinger, R. Di Leonardo, H. Löwen, C. Reichardt, G. Volpe, and G. Volpe, *Rev. Mod. Phys.* **88**, 045006 (2016).
- [3] E. Fodor and M. Marchetti, *Physica A* **504**, 106 (2018).
- [4] S. Ramaswamy, *J. Stat. Mech.: Theory Exp.* (2017) 054002.
- [5] M. J. Bowick, N. Fakhri, M. C. Marchetti, and S. Ramaswamy, *Phys. Rev. X* **12**, 010501 (2022).
- [6] A. Cavagna, S. M. D. Queirós, I. Giardina, F. Stefanini, and M. Viale, *Proc. R. Soc. Ser. B Biol. Sci.* **280**, 20122484 (2013).
- [7] T. Vicsek and A. Zafeiris, *Phys. Rep.* **517**, 71 (2012).
- [8] J. Tailleur and M. E. Cates, *Phys. Rev. Lett.* **100**, 218103 (2008).
- [9] J. Tailleur and M. E. Cates, *Europhys. Lett.* **86**, 60002 (2009).
- [10] S. Wang and P. G. Wolynes, *Proc. Natl. Acad. Sci. USA* **108**, 15184 (2011).
- [11] S. J. Ebbens and J. R. Howse, *Soft Matter* **6**, 726 (2010).
- [12] J. R. Howse, R. A. L. Jones, A. J. Ryan, T. Gough, R. Vafabakhsh, and R. Golestanian, *Phys. Rev. Lett.* **99**, 048102 (2007).
- [13] H.-R. Jiang, N. Yoshinaga, and M. Sano, *Phys. Rev. Lett.* **105**, 268302 (2010).
- [14] D. Yamada, T. Hondou, and M. Sano, *Phys. Rev. E* **67**, 040301(R) (2003).
- [15] V. Narayan, S. Ramaswamy, and N. Menon, *Science* **317**, 105 (2007).
- [16] K. Cheng, P. Liu, M. Yang, and M. Hou, *Soft Matter* **18**, 2541 (2022).
- [17] A. Murali, P. Dolai, A. Krishna, K. V. Kumar, and S. Thutupalli, *Phys. Rev. Res.* **4**, 013136 (2022).
- [18] L. Walsh, C. G. Wagner, S. Schlossberg, C. Olson, A. Baskaran, and N. Menon, *Soft Matter* **13**, 8964 (2017).
- [19] C. Tapia-Ignacio, L. L. Gutierrez-Martinez, and M. Sandoval, *J. Stat. Mech.: Theory Exp.* (2021) 053404.
- [20] F. Donado, R. E. Moctezuma, L. López-Flores, M. Medina-Noyola, and J. L. Arauz-Lara, *Sci. Rep.* **7**, 12614 (2017).
- [21] F. J. Sevilla and L. A. Gómez Nava, *Phys. Rev. E* **90**, 022130 (2014).
- [22] J. Deseigne, S. Léonard, O. Dauchot, and H. Chaté, *Soft Matter* **8**, 5629 (2012).
- [23] C. Tapia-Ignacio, J. Garcia-Serrano, and F. Donado, *Phys. Rev. E* **94**, 062902 (2016).
- [24] C. Tapia-Ignacio, R. E. Moctezuma, F. Donado, and E. R. Weeks, *Phys. Rev. E* **102**, 022902 (2020).
- [25] M. Ledesma-Motolinía, J. Carrillo-Estrada, and F. Donado, *Sci. Rep.* **11**, 16531 (2021).
- [26] F. C. Meldrum and C. O'Shaughnessy, *Adv. Mater.* **32**, 2001068 (2020).
- [27] G. Jung and C. F. Petersen, *Phys. Rev. Res.* **2**, 033207 (2020).
- [28] K. Martens, L. Angelani, R. Di Leonardo and L. Bocquet, *Eur. Phys. J. E* **35**, 84 (2012).
- [29] R. Soto and R. Golestanian, *Phys. Rev. E* **89**, 012706 (2014).
- [30] N. Sepúlveda and R. Soto, *Phys. Rev. E* **94**, 022603 (2016).
- [31] M. Barriuso Gutiérrez, C. Vanhille-Campos, F. Alarcón, I. Pagonabarraga, R. Brito, and C. Valeriani, *Soft Matter* **17**, 10479 (2021).
- [32] S. Goldstein, *Q. J. Mech. Appl. Math.* **4**, 129 (1951).
- [33] P. Romanczuk, M. Bär, W. Ebeling, B. Lindner, and L. Schimansky-Geier, *Eur. Phys. J. Spec. Top.* **202**, 1 (2012).
- [34] F. J. Sevilla, *Phys. Rev. E* **101**, 022608 (2020).
- [35] F. J. Sevilla and M. Sandoval, *Phys. Rev. E* **91**, 052150 (2015).
- [36] P. Castro-Villarreal and F. J. Sevilla, *Phys. Rev. E* **97**, 052605 (2018).
- [37] M. E. Cates and J. Tailleur, *Europhys. Lett.* **101**, 20010 (2013).
- [38] F. J. Sevilla and P. Castro-Villarreal, *Phys. Rev. E* **104**, 064601 (2021).
- [39] C. Kurzthaler, C. Devailly, J. Arlt, T. Franosch, W. C. Poon, V. A. Martinez, and A. T. Brown, *Phys. Rev. Lett.* **121**, 078001 (2018).
- [40] A. Escobar, F. Donado, R. E. Moctezuma, and E. R. Weeks, *Phys. Rev. E* **104**, 044904 (2021).
- [41] G. Torres-Vargas, R. Fossion, F. Donado, F. López-González and C. Tapia-Ignacio, *Sci. Rep.* **10**, 11474 (2020).
- [42] M. Sánchez-Miranda, J. Carrillo-Estrada, and F. Donado, *Sci. Rep.* **9**, 3531 (2019).
- [43] This equation has been used frequently in relativistic diffusion theory, whose applications appear in different contexts ranging from high energy collisions experiments, diffusion of light through turbid media, among others (see Refs. [48,49] and the references therein).
- [44] P. Castro-Villarreal, A. Villada-Balbuena, J. M. Méndez-Alcaraz, R. Castañeda-Priego, and S. Estrada-Jiménez, *J. Chem. Phys.* **140**, 214115 (2014).
- [45] P. Castro-Villarreal, *J. Stat. Mech.: Theory Exp.* (2014) P05017.
- [46] A. Villada-Balbuena, A. Ortiz-Ambriz, P. Castro-Villarreal, P. Tierno, R. Castañeda-Priego and J. M. Méndez-Alcaraz, *Phys. Rev. Res.* **3**, 033246 (2021).
- [47] L. Apaza and M. Sandoval, *Soft Matter* **14**, 9928 (2018).
- [48] J. Dunkel and P. Hänggi, *Phys. Rep.* **471**, 1 (2009).
- [49] G. H. Weiss, *Physica A* **311**, 381 (2002).